ADVANCED FUNCTIONAL MATERIALS
www.afm-journal.de

Accelerating the Laser-Induced Phase Transition in Nanostructured FeRh via Plasmonic Absorption

M. Mattern, J.-E. Pudell, J. A. Arregi, J. Zlámal, R. Kalousek, V. Uhlíř, M. Rössle, and M. Bargheer**

By ultrafast x-ray diffraction (UXRD), it is shown that the laser-induced magnetostructural phase transition in FeRh nanoislands proceeds faster and more complete than in continuous films. An intrinsic 8 ps timescale is observed for the nucleation of ferromagnetic (FM) domains in the optically excited fraction of both types of samples. For the continuous film, the substrate-near regions are not directly exposed to light and are only slowly transformed to the FM state after heating above the transition temperature via near-equilibrium heat transport. Numerical modeling of the absorption in the investigated nanoislands reveals a strong plasmonic contribution near the FeRh/MgO interface. The larger absorption and the optical excitation of the electrons in nearly the entire volume of the nanoislands enables a rapid phase transition throughout the entire volume at the intrinsic nucleation timescale.

1. Introduction

Reducing the structure-size of metallic ferromagnets to the nanoscale not only helps increasing the information storage density but also enables direct plasmonic coupling of light to the magnetic nano-bit for magnetoplasmonic control and readout.[1,2] This is a particularly exciting perspective in the context of femtosecond optomagnetism[3] with ultrafast optical manipulation of magnetic properties such as a polarization control of two magnetic nanolayers mediated by plasmon-polaritons[4] and plasmonic enhanced all-optical switching in magnetic nanodisks.[5,6] Heat assisted magnetic recording (HAMR)[7,8] already uses plasmonic near fields to confine the optical energy to sub-wavelength areas for highly local magnetic switching in the new generation of magnetic hard drives. In nano-granular FePt films constituting the classical HAMR material recent experiments confirm a plasmonically enhanced ultrafast switching.[9]

In the context of HAMR, it has been proposed that the write process in FePt media could be further assisted in FeRh/FePt exchange spring bilayers by utilizing the thermally induced antiferromagnetic-to-ferromagnetic (AF-FM) phase transition in FeRh around 370 K.[10] FeRh and its first-order phase transition accompanied with a gigantic lattice expansion and a magnetoresistance have been focus of extensive research with perspective on applications in spintronics, nanoscale sensing, or solid-state magnetocaloric refrigeration.[11–14] The tunability of the transition temperature by growth-induced strain and chemical doping,[11] as well as the active electric-field control of the magnetization and the electric resistivity via the strain of ferroelectrics[12,13] make FeRh promising for future applications.

The potential consequences of nanostructuring FeRh go well beyond plasmonic coupling. Lateral nanostructuring limits the number of independent nucleation sites, which changes the nature of magnetization reversal from multi-domain to single-domain and results in discrete avalanche-like jumps of the order parameter upon cooling.[15,16] In thermal equilibrium, the phase transition crucially depends on the lattice structure. The tetragonal distortion of the unit cell originating from an in-plane substrate-induced compression enhances the transition temperature.[16–18] In FeRh nanoislands, the partial relaxation of this tetragonal distortion reduces the transition temperature.[16,19] Generally, in-plane nano-structuring unlocks

M. Mattern, J.-E. Pudell, M. Bargheer
Institut für Physik und Astronomie
Universität Potsdam
14476 Potsdam, Germany
E-mail: bargheer@uni-potsdam.de
J.-E. Pudell, M. Rössle, M. Bargheer
Helmholtz-Zentrum Berlin für Materialien und Energie GmbH
Wilhelm-Conrad-Röntgen Campus, BESSY II
12489 Berlin, Germany
J.-E. Pudell
European XFEL
22869 Schenefeld, Germany
J. A. Arregi, J. Zlámal, R. Kalousek, V. Uhlíř
CEITEC BUT
Brno University of Technology
Brno 61200, Czech Republic
E-mail: arregi@vutbr.cz
J. Zlámal, R. Kalousek, V. Uhlíř
Institute of Physical Engineering
Brno University of Technology
Brno 61669, Czech Republic

The ORCID identification number(s) for the author(s) of this article can be found under https://doi.org/10.1002/adfm.202313014

DOI: 10.1002/adfm.202313014

in-plane expansion on the picosecond timescale in contrast to the exclusive out-of-plane expansion of laser-excited continuous thin films.[20] The 3D nature of the picosecond strain response of nanoislands preserves bulk-like material-specific expansion properties and results in a complex strain response due to cross-talk of in- and out-of-plane expansion via the Poisson effect.[21–24]

Previous experiments studied the laser-induced phase transition in FeRh by the emergence of magnetization,[25–28] changes in the electronic structure,[29] spin currents injected into adjacent metals[30] and the rise of the larger FM lattice constant.[31–33] Probing the structural order parameter by ultrafast x-ray diffraction (UXRD), we recently disentangled optically induced nucleation and heat-transport driven propagation of the FM phase in inhomogeneously excited FeRh continuous films, whose thickness exceeds the optical penetration depth.[33] We identified a universal 8 ps nucleation timescale in FeRh, which does not depend on the film thickness and temperature nor on applied laser fluence and magnetic field.[33] The effects of nanostructuring on the coupled ultrafast dynamics of demagnetization,[23] remagnetization,[34] and strain[21–23] have been thoroughly studied for FePt. Ultrafast experiments on FeRh nanoislands that study the influence of the in-plane expansion, reduced number of nucleation sites and plasmonic excitation are lacking up to now.

Here, we use UXRD to explore the kinetics of the laser-driven phase transition in FeRh nanoislands by probing the ultrafast emergence of a larger lattice constant that parameterizes the FM phase as structural order parameter. In order to access the effect of finite lateral dimensions, we compare the results to a similarly thick continuous FeRh film as reference. In the nanoislands, the AF-FM phase transition drives a partial in-plane expansion of the nanoislands both in equilibrium and on ultrafast timescales. Upon laser excitation, we observe the same 8 ps nucleation timescale in both samples indicating an intrinsic property of the optically induced phase transition irrespective of the sample morphology. However, while we observe a relatively slow heat transport-driven growth of the FM phase into the depth of the continuous film, the phase transition of the nanostructured film occurs precisely on the intrinsic timescale of domain nucleation. By modeling the absorption of the nanostructures, we relate this acceleration of the phase transition to a homogeneous optical excitation of the electrons in FeRh along the out-of-plane dimension due to plasmonic effects enabled by the size of the metallic islands below the excitation wavelength.

2. AF-to-FM Phase Transition in Equilibrium

In the first step, we characterize the morphology dependence of the AF-FM phase transition of FeRh in thermal equilibrium as a reference for the time-resolved experiments. **Figure 1** compares the properties of the phase transition of a continuous 55 nm thick FeRh(001) film with a lateral nanostructured film with a mean height of 52 nm. Figure 1a,b schematically sketch the sample structures grown on MgO(001) substrates.

Figure 1c,f displays the diffracted intensity around the (002) FeRh Bragg peak along the out-of-plane reciprocal space coordinate q_z recorded at the KMC-3 XPP endstation at BESSY II in the low-alpha operation mode[35] with monochromized 9 keV hard x-ray photons. With increasing temperature, we observe the emergence of an additional Bragg peak at smaller q_z values that correspond to the arising FM phase when the temperature approaches the mean transition temperature of the thin film (370 K) and the nanoislands (350 K), respectively. The integrated intensity of this Bragg peak is directly proportional to the volume of FeRh exhibiting the FM phase[31] and thus parameterizes the FM phase during the temperature-driven AF-FM phase transition. The proportion of the FM Bragg peak in the total intensity yields the temperature-dependent FM volume fraction V_{FM}. Figure 1d,g compares this structural parameterization of the phase transition (symbols) to the macroscopic magnetization normalized to its maximum (solid lines) serving as complementary order parameter of the FM phase. Note, the heterogeneous transition temperature at different sample sites broadens the thermal hysteresis of the magnetization with respect to the locally probed structural order parameter.

The comparison of the two samples reveals a dependence of the AF-FM phase transition in thermal equilibrium on the sample morphology. The enhanced surface-to-volume ratio of the nanoislands results in a noticeable residual FM phase that persists below the transition temperature T_T at the symmetry breaking surface[36] and at the film-substrate interface.[37] In addition, the small lateral extent of the islands partially relaxes the substrate-induced tetragonal distortion of FeRh, which lowers the transition temperature for the nanoislands.[16,17,19] This is indicated by the lower mean out-of-plane lattice constant d with respect to the continuous film (see Figure 1e,h) given by the center-of-mass (COM) of the diffracted intensity via $d = 4\pi/q_{z,\,COM}$. This applies in particular to the out-of-plane expansion associated with the phase transition. While, we find 0.4% expansion for the nanoislands close to the bulk value of 0.3%,[38] the substrate-induced clamping of the in-plane expansion suppresses the Poisson effect[20] and results in an out-of-plane expansion of 0.6% for the thin film. We quantified this morphology-dependent in-plane clamping by modelling the temperature-dependent lattice constant in Figure 1e,h (symbols). Utilizing literature values for the thermal expansion of FeRh and MgO, Equation (2) (solid lines) yields excellent agreement if the thin film purely follows the in-plane expansion of the MgO substrate and if 58% of the volume of the nanoislands behave bulk-like where the relaxation of the in-plane constraints is expected to increase toward the surface and to depend on the in-plane dimensions of the different nanoislands[39] (see Experimental Section).

3. Ultrafast Phase Transition Tracked by UXRD

In the UXRD experiment, we track the emergence of the FM Bragg peak upon excitation by a 600 fs near-infrared laser pulse. The time-dependent integral of the FM Bragg peak quantifies the transient laser-induced FM volume fraction V_{FM}. **Figure 2**a,b displays the diffracted intensity along q_z before and after an excitation with 11.2 mJcm^{-2} at 340 K for the thin film and with 5.2 mJcm^{-2} at 230 K for the nanoislands, respectively. The emerging FM Bragg peaks indicate the optically induced AF-FM phase transition for both samples. The AF and FM Bragg peaks are well separated for the thin film. For the nanoislands, an ultrafast in-plane expansion on short timescales is enabled by their small lateral extent.[20] The concomitant transient out-of-plane Poisson-contraction results in less separated Bragg peaks (Figure 2b) for the nanoislands. This indicates a reduced tetragonal distortion

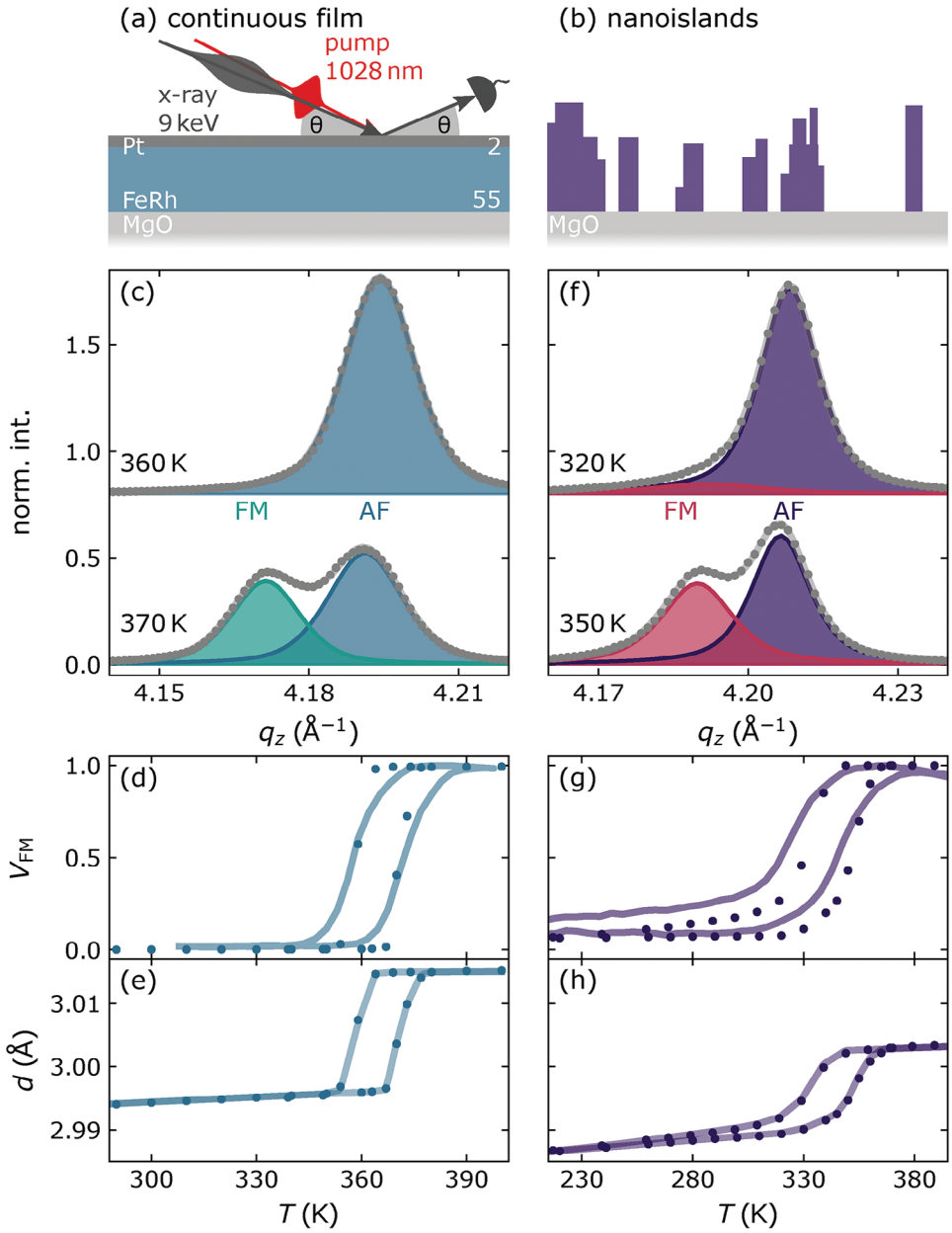

Figure 1. Morphology-dependent phase transition in thermal equilibrium: Schematic of the UXRD experiment mapping the reciprocal space via $\theta - 2\theta$-scans and the sample structure of the continuous film (a) and a sketch of the nanoislands (b). Panels (c–e) and (f–h) characterize the equilibrium AF-FM phase transition in the continuous film and the nanostructures, respectively. c, f) The diffracted intensity (grey symbols) is the superposition of an AF and an arising FM Bragg peak at a larger out-of-plane lattice constant during heating above T_T. d, g) Temperature-dependent ferromagnetic volume fraction V_{FM} determined by the relative integrated intensity of the FM Bragg peak (symbols) as structural order parameter and the magnetization normalized to its maximum value as magnetic order parameter (solid lines). e, h) Temperature-dependent lattice constant (symbols) modeled by Equation (2) using bulk expansion parameters (solid lines).

of the unit cell upon laser-excitation and the emergence of more cubic FM unit cells upon nucleation in the nanoislands, as already discussed for thermal equilibrium. In addition to the lattice constant change across the phase transition, the dynamics of the laser-induced phase transition also depends on the sample morphology. While the integrated intensity of the FM Bragg peak barely changes between 40 and 240 ps for the nanoislands, the FM Bragg peak clearly increases after 40 ps for the thin film.

Figure 3 displays the resulting transient FM volume fraction V_{FM} for both samples under various excitation conditions (symbols). For the nanoislands, we observe an exponential rise of V_{FM} associated with an optically induced nucleation of FM domains[31,33] according to:

$$V_{FM}(t) = V^*_{FM} \cdot \left(1 - e^{-t/\tau}\right) \quad (1)$$

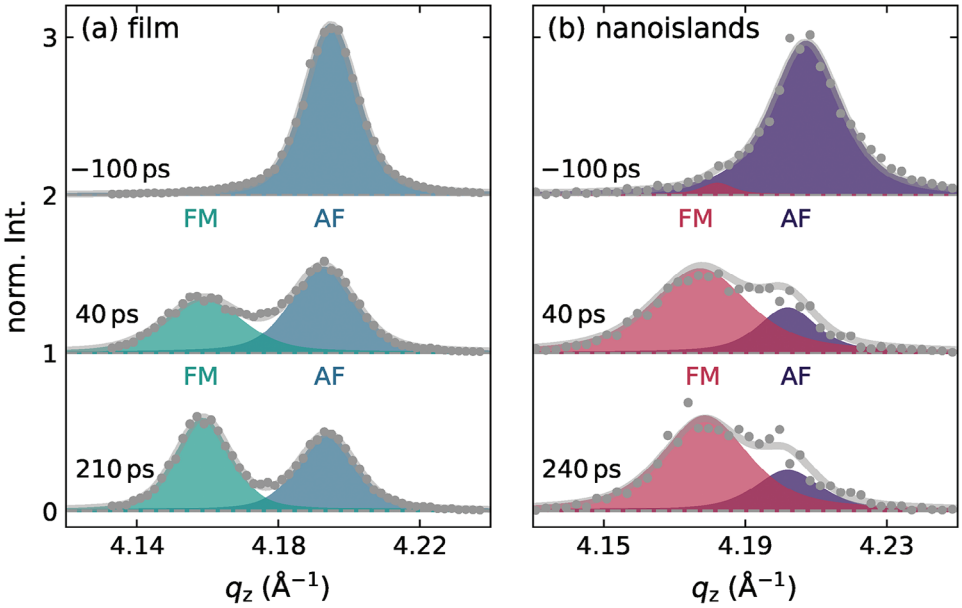

Figure 2. Morphology-dependent tetragonal distortion across the laser-induced phase transition: a) Transient Bragg peaks of the thin film for an excitation of 11.2 mJcm^{-2} at 340 K dissected into the FM (green) and AF (blue) Bragg peak that are well-separated in reciprocal space. b) In the nanoislands, the FM (pink) and AF (purple) Bragg peak are less separated due to the partial in-plane expansion of the unit cell across the laser-induced phase transition for 5.2 mJcm^{-2} at 230 K. The data for different pump-probe delays are vertically off-set to improve visibility.

with the universal nucleation timescale $\tau = 8$ ps previously identified for thin films.[33] The convolution of the exponential growth according to Equation (1) with the 17 ps-long x-ray pulse limiting the time-resolution (solid lines) yields an excellent agreement with the experimental $V_{FM}(t)$ of the nanoislands in Figure 3a,b. The final FM volume fraction V^*_{FM} is adjusted to the experimental value of $V_{FM}(t = 40\,\text{ps})$ for the respective measurement and we include the residual FM phase in Figure 1g being present before excitation. With increasing fluence and initial sample temperature a larger fraction of the nanoislands volume is excited above the critical threshold characteristic for the first-order phase transition,[26,31] which results in an enhanced V^*_{FM}.

For the continuous thin film, we observe a strong dependence of the rising V_{FM} on the initial sample temperature (see Figure 3c,d). At 260 K the FM volume fraction rises on the same timescale as in the nanoislands and reaches its maximum within 40 ps. For higher temperatures, we observe an additional slow rise of V_{FM} after 40 ps. The amplitude of this additional contribution, as well as its timescale depend on the fluence and temperature. We recently associated this delayed rise with a propagation of the FM phase into the depth of the inhomogeneously excited film (see **Figure** 4f) via near-equilibrium heat transport that heats the substrate-near part above the transition temperature.[33] Additionally, we showed that the propagation of the FM phase is slower than expected from the equilibrium heat transport. Here, we nicely capture the experimental fluence- and temperature-dependent $V_{FM}(t)$ by a straight forward model (solid lines in Figure 3c,d),which keeps the nucleation timescale fixed in all graphs of Figures 3. The model describing additional dynamics of V_{FM} in Figures 3c,d beyond 40 ps considers the heating of FeRh above the transition temperature calculated by solving the 1D heat diffusion equation using literature values of the thermophysical parameters. Further details are given in the Experimental Section 6. The excellent simultaneous agreement with both the fluence- and temperature-dependent rising dynamics and amplitudes with a fixed set of parameters verifies our interpretation of a propagation of the FM phase into the depth of the inhomogeneously excited thin film via heat diffusion.

In addition to this morphology-dependent dynamics of V_{FM}, Figure 3a,b show that a fluence of 6.2 mJcm^{-2} induces the FM phase in nearly the complete volume of the FeRh nanoislands within 40 ps. In contrast, Figure 3c,d shows that nearly twice the fluence only transforms 35% of the continuous thin film within 40 ps. After 40 ps the FM volume fraction continues to rise slowly, however not beyond 60%. This comparison unambiguously demonstrates that the laser-induced AF-FM phase transition in laterally nanostructured FeRh is faster and more complete compared to the continuous thin film. This observation cannot be explained by the additional 2 nm Pt capping layer of the continuous film that only reduces the absorption in FeRh by ≈10 %.

4. Modeling the Absorbed Light Power by Classical Electrodynamics

To explain the observed morphology dependence of the laser-induced AF-FM phase transition, we calculate the local energy dissipation in the nanoislands by classical electrodynamics (see Experimental Section 6 for further details). To describe the experiment as realistically as possible we reproduce the topography of the irregularly shaped nanoislands characterized by atomic force microscopy (AFM) (Figure 4a) by ellipsoids (see Figure 4b).

Figure 4c displays the calculated local power absorption P_{abs} of the nanostructures for the excitation conditions in the experiment, i.e., p-polarized light with a wavelength of 1028 nm

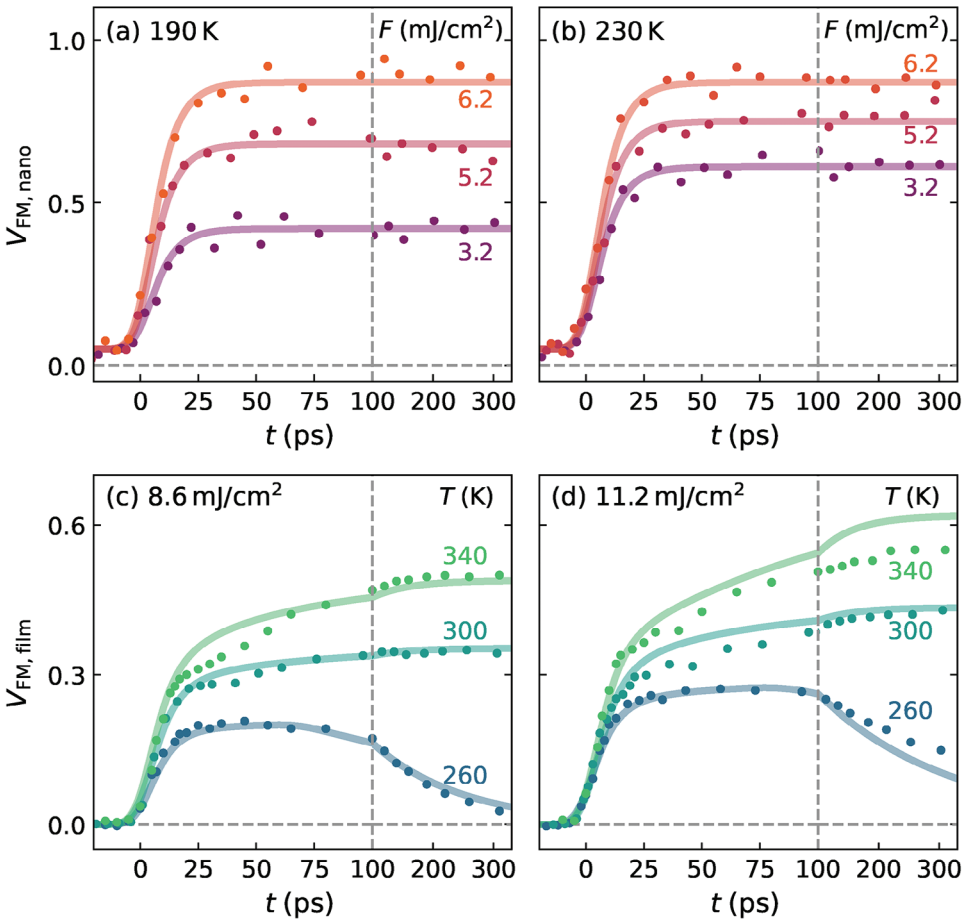

Figure 3. Morphology-dependent dynamics of the laser-induced FM volume fraction: a) Transient FM volume fraction of the nanoislands at $T = 190$ K for various fluences F. b) Same for $T = 230$ K, which increases the conversion to the FM state at low fluence. c) Temperature series at a relatively low fluence of $F = 8.6\,\mathrm{mJcm^{-2}}$ for the thin film. d) Same for $F = 11.2.0\,\mathrm{mJcm^{-2}}$. The two-step rise of V_{FM} in the thin film (c and d) indicates propagation of the nucleated FM phase into the depth of the layer driven by near-equilibrium heat transport. In (a,b), solid lines denote the kinetics of FM domain nucleation according to Equation (1) convoluted with the time-resolution given by the duration of the x-ray pulse. The solid lines in (c,d) represent the modelled $V_{FM}(t)$ considering the time-dependent heating above $T_{AF\text{-}FM}$ via heat diffusion (see Section 6 for further details). The vertical dashed lines denote a break in the delay axis.

incident under 60° with respect to the sample normal. The calculated local power absorption P_{abs} reveals the existence of hot-spots with drastically enhanced absorption. By fitting an exponential decay function to the local z-dependent absorption (FeRh-MgO interface corresponds to $z = 0$), we find a large spread of the optical penetration depth δ_p. Figure 4d shows this distribution relative to the semi-infinite medium value $\delta_{p,0} = 14.7$ nm, that also applies to the continuous film. Yellow color-code indicates a locally strongly enhanced optical penetration depth due to nanostructuring that leads to a more homogeneous excitation along z. Figure 4e depicts an exemplary z-dependent cross section of the absorption as function of the in-plane x coordinate at $y = 3.2\,\mu$m. This lineout displays an enhanced absorption near the FeRh-MgO interface in several nanoislands indicated by the yellow color.

To compare these results to a continuous film, we determine the average total absorption in the nanoislands as function of the distance from the FeRh-MgO interface ($z = 0$) from the local power absorption $P_{abs}(x, y)$ in Figure 4c. Figure 4f displays the average z-dependent absorption of the nanoislands (symbols) and of a 55 nm continuous FeRh film scaled by the surface coverage of the nanoislands (49%) in the studied sample (grey solid line). This comparison highlights a more homogeneous excitation of the nanoislands and a strong enhancement of the absorption in the substrate-near region that is barely excited in the continuous thin film despite the comparable average height of the nanoislands. Comparing the z-integrated absorption of the nanoislands and the continuous film in Figure 4f, we find that the total optical absorption of the nanostructures amounts to 34% of the incident power, which exceeds the absorption of the continuous FeRh film by a factor of 1.5.

5. Plasmonic Absorption

The enhanced absorption near the FeRh-MgO interface[40] responsible for the local absorption hot-spots shown in Figure 4c is characteristic of localized surface plasmons (LSPs).[41,42] The associated resonance in the absorption spectrum crucially depends

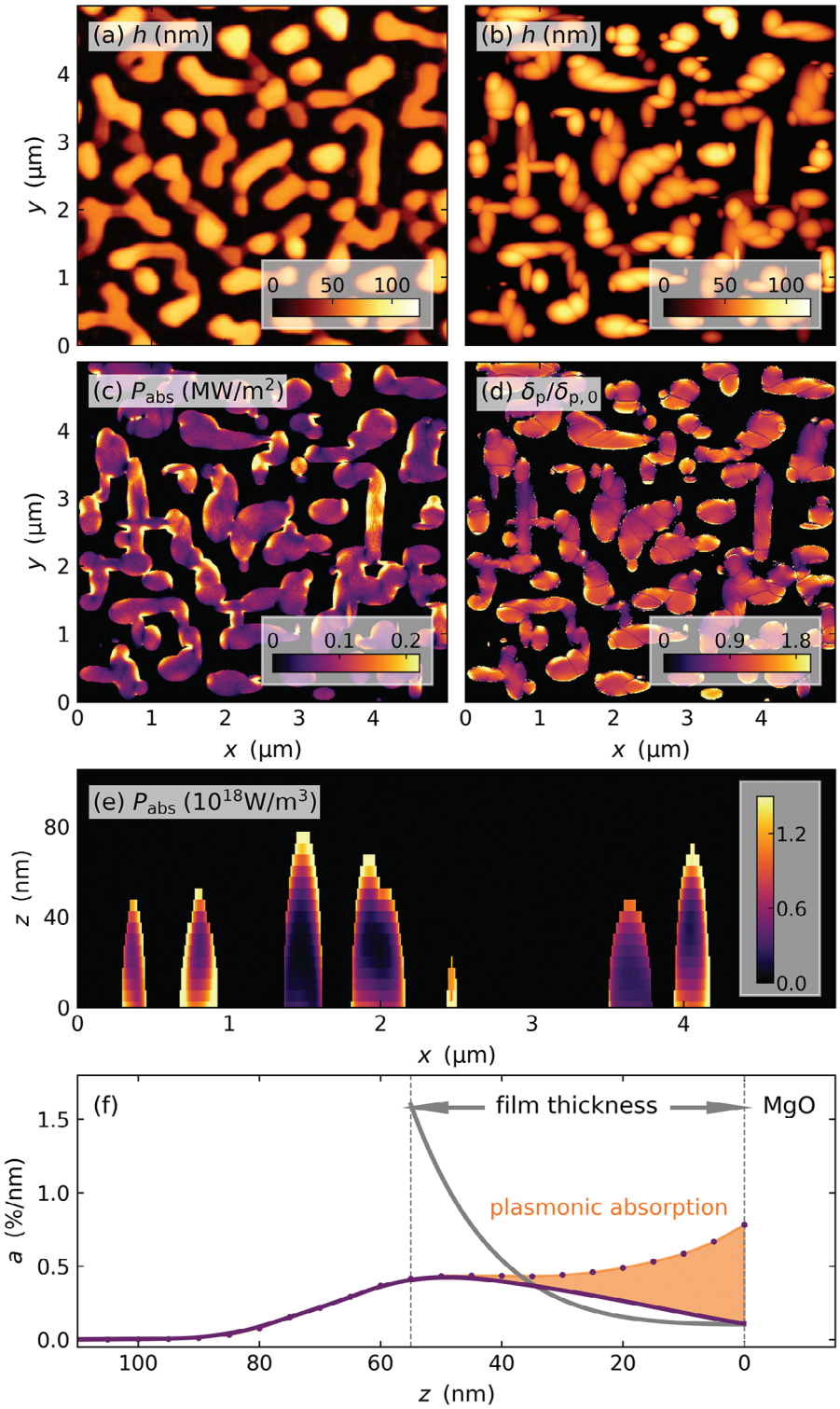

Figure 4. Depth-dependent optical excitation of nanostructured FeRh: Re-build of the topography of the FeRh nanostructures characterized by AFM (a) in COMSOL (b). The AFM data are the same as in our previous publication[19] since we use the identical sample in this study. c) Calculated local absorbed power per area of the FeRh nanostructures by solving the Maxwell equations for $\lambda = 1028$ nm. d) Local optical penetration depth determined from P_{abs} as function of the depth relative to the semi-infinite medium value $\delta_{p,0} = 14.7$nm. e) Absorption of different nanoislands as function of z at $y = 3.2\,\mu$m. f) Total absorption profile integrated over all pixels (purple symbols). The purple solid line corresponds to the hypothetical scenario of z-dependent absorption integrated over all pixels, for each assuming an absorption profile of a continuous film of an equivalent thickness given by $\delta_{p,0}$. The grey line denotes the absorption profile of the continuous 55 nm thick FeRh film. The orange shaded area represents the effect of the plasmonic absorption in the nanoislands.

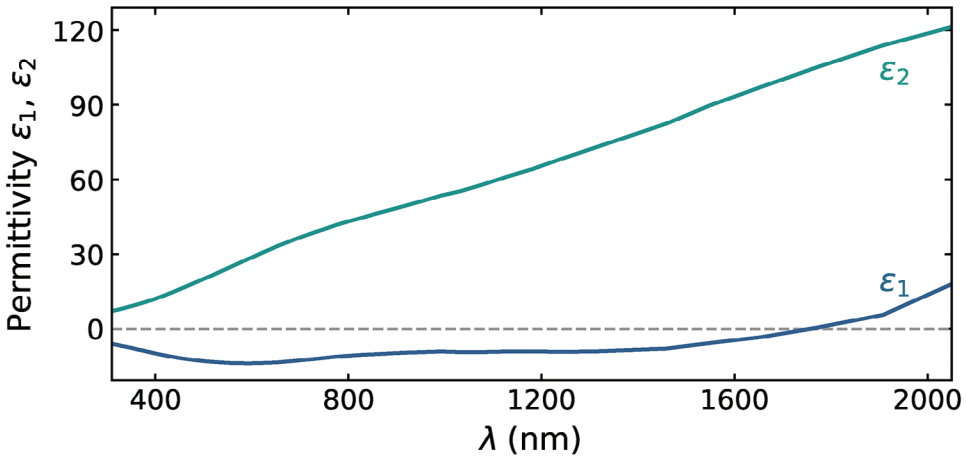

Figure 5. Spectral ellipsometry results for the complex dielectric function $\varepsilon_1 + i\varepsilon_2$ of a 30 nm-thick continuous FeRh film. The negative ε_1 for wavelength between 300 and 1800 nm demonstrates that FeRh supports LSPs for a broad range of excitation wavelength around the pump wavelength of 1028 nm used in the UXRD experiment.

on the spatial dimensions of the nanostructures. Changing the diameter of metal nanodiscs with constant height shifts the resonance across the entire visible and near-infrared spectrum for various metals.[43] An additional red shift and concomitant broadening is observed when changing the aspect ratio of ellipsoids at constant volume.[44] The distribution of nanoislands in our FeRh sample is both inhomogeneous in size and aspect ratio, which leads to an ultrabroad featureless absorption spectrum. Nonetheless, the plasmonic absorption mediated by the nanoscale size of a metal and characterized by a negative permittivity (see **Figure 5**) is central to explain the large amount of light energy dissipated near the FeRh-MgO interface, i.e., at depths that receive only a negligible amount of light energy in continuous thin films.

The calculated z-dependent absorption of the nanoislands in Figure 4f contains signatures of both the dissipation of light energy via plasmons and the local FeRh height that relates a single height z to different depth relative to the local surface. In order to isolate the contribution from the plasmonic absorption, we calculate the z-dependent absorption of the nanoislands sample by assuming that the absorption of each pixel is identical to that of a continuous film of a thickness equivalent to the local FeRh height. Thus, the z-dependent absorption for each pixel is determined by the semi-infinite medium value of the optical penetration depth $\delta_{p,0}$ starting at the local height. The sum over all pixels yields the purple solid line in Figure 4f that matches the COMSOL simulation for $z > 50$ nm where the absorption decreases with increasing z because only nanoislands higher than the z value contribute to absorption. However, the average absorption of nanostructures (symbols) for $z < 30$ nm is much larger than that predicted by the pixel-integrated absorption of equivalent thin films, which neglects the plasmonic enhancement near the FeRh-MgO interface.

This difference highlighted by the orange shaded area originates from the plasmonic absorption that increases the absorption beyond integration of a local Lambert-Beer exponential decay. It enhances the absorption near the FeRh-MgO interface where the plasmonic absorption is particularly strong because the dielectric response of the substrate enhances the field. This additional dissipation of the light energy in the nanoislands leads to a more homogeneous optical excitation along the z direction with respect to continuous thin films. Additionally, Figure 4f displays that the plasmonic absorption significantly increases the total absorption of the nanoislands.

This increased and more homogeneous plasmonic excitation, which mediates effectively a localized absorption of photons, is the key to enable the non-equilibrium pathway of the phase transition in FeRh that was previously assigned to an 8 ps timescale for the nucleation of ferromagnetic domains upon direct photoexcitation.[33] In the continuous thin film, the ferromagnetic phase only emerges in the optically excited near-surface region on the fast 8 ps timescale - probably induced by a rapid modification of the electronic band structure[29] -, while the ferromagnetic phase only rises on a 60 ps timescale in the lower lying regions after heating above the transition temperature via near-equilibrium heat transport. Therefore, enabling the non-equilibrium pathway of the transition in the entire volume of the nanoislands, plasmonic absorption drastically accelerates the laser-induced phase transition in FeRh that is even more efficiently driven due to the overall enhanced absorption.

6. Conclusion

In summary, we studied the morphology dependence of the laser-induced AF-FM phase transition by comparing a continuous and a nanostructured thin FeRh film. We find an ultrafast in-plane expansion of the nanoislands, whereas the thin FeRh film is pinned to the MgO. This results in a less tetragonal distortion of the unit cell across the phase transition, however, it has no influence on the nucleation timescale of the FM domains. Instead, only the change of the absorption profile due to plasmons affects the dynamics of the phase transition: By modelling the spatially resolved optical absorption of the FeRh nanostructures, we identified an enhanced absorption near the FeRh-MgO interface and an enhanced optical penetration depth. This results in a

homogeneous excitation of the nanoislands, which drives a nucleation of FM domains on an 8 ps timescale within the volume of the FeRh nanostructures. This accelerates the phase transition in comparison with the continuous film that exhibits nucleation only within the optically excited near-surface region and shows a subsequent slow growth of the FM phase into the depth of film at initial sample temperatures slightly below the transition temperature.

7. Experimental Section

Sample Growth and Characterization: The continuous 55 nm thick FeRh(001) film was grown by magnetron sputtering from an equiatomic FeRh target[17] and capped by 2 nm of Pt. The nanostructured sample was composed of epitaxial FeRh(001) nanoislands formed by solid state dewetting of an 20 nm-thick epitaxial FeRh(001) film via self-assembly resulting in maze-like structures[19] with a mean height of 52 nm. The sample was the same as in the previous publication that also shows larger area scanning electron microscopy images.[19] The magnetization was measured via vibrating sample magnetometry using a QuantumDesign VersaLab magnetometer. AFM topography measurements were performed using a Dimension Icon microscope from Bruker Corporation while employing commercial MESP probes. Figure 5 displays the complex dielectric function of a 30 nm-thick continuous FeRh film as function of the wavelength λ experimentally determined via ellipsometry. Literature consistently reports a negative value of the real part ε_1 for the visible an near infrared, with spectral details depending on sample preparation.[45–47]

UXRD Experiment: The FeRh samples are excited by 600 fs p-polarized pump pulses with a central wavelength of 1028 nm and a repition reate of 100 kHz that were incident at ≈30° with respect to the sample surface as sketched in Figure 1a. The footprint of the pump pulse on the sample was 1300 × 900 µm^2 (major and minor FWHM-diameter), which was *nine* times larger than the footprint of the x-ray probe pulse (400 × 300 µm^2) to ensure a laterally homogeneous excitation of the probed volume. The emergence of the FM Bragg peak that parameterizes the laser-induced AF-FM phase transition was probed by 9 keV hard x-ray pulses with a pulse duration of 17 ps[35] performing symmetric $\theta - 2\theta$ scans around the (002) Bragg reflection at 28°. The diffracted x-rays were recorded on an area detector (Dectris PILATUS 100K).

Modelling d(T) in Equilibrium: The influence of the substrate-induced in-plane clamping on the out-of-plane expansion of the FeRh samples is described by:[20]

$$\alpha_{\text{eff}} = \alpha_{\text{bulk}}(T) + 2\chi\frac{c_{1133}}{c_{3333}}\left(\alpha_{\text{bulk}}(T) - \alpha_{\text{MgO}}\right) \quad (2)$$

where $\alpha_{\text{bulk}}(T)$ and $\alpha_{\text{MgO}} = 10.5 \cdot 10^{-6}\text{K}^{-1}$ denote the thermal expansion coefficients of bulk FeRh and MgO, respectively. The expansion of FeRh $\alpha_{\text{bulk}}(T)$ is given by the expansion coefficients $\alpha^{\text{FM}} = 6.0 \cdot 10^{-6}\text{K}^{-1}$ and $\alpha^{\text{AF}} = 9.7 \cdot 10^{-6}\text{K}^{-1}$ in the AF and FM phase[48] and the expansion of 0.3% across the AF-FM phase transition,[38] considering the temperature-dependent volume fraction in the FM phase $V_{\text{FM}}(T)$, the derivation is based on the integrated intensity of the FM Bragg peak in Figure 1c,f. The elastic constants of FeRh c_{1133} and c_{3333} quantify the effect of the in-plane expansion on the out-of-plane expansion via the Poisson effect[20] and α_{eff} denotes the modified expansion coefficient of the samples depending on the parameter χ. This parameter measured the epitaxy to the substrate, where $\chi = 0$ corresponds to pure bulk-like in-plane expansion and $\chi = 1$ to an in-plane expansion completely determined by the MgO substrate. Excellent agreement was found for $\chi = 1$ and $\chi = 0.42$ for the continuous film and the nanoislands, respectively.

Modelling $V_{FM}(t)$ in the Continuous Film: In order to describe the fluence- and temperature-dependent additional slow rise of V_{FM} in Figure 3c,d, the heat transport was explicitly considered within the inhomogeneously excited FeRh film ($\delta_{p,0} = 14.7$ nm) by solving the 1D heat diffusion equation utilizing literature values of the thermo-physical properties of Pt, FeRh, and MgO as described previously.[33] V_{FM} was assumed to rise on the 8 ps nucleation timescale in the fraction of the FeRh film that is heated above the average AF-FM transition temperature $T_{\text{AF-FM}} = 370$ K (see Figure 1e) directly after the excitation ($t < 200$ fs). This already yields excellent agreement for the measurements at 260 K within the first 50 ps. In order to obtain a good fit for the delayed rise of V_{FM} by heat transport, an exponential rise on a 60 ps timescale was assumed after the local temperature exceeds $T_{\text{AF-FM}}$ at larger delays due to the heat transport. To match the decrease of V_{FM}, i.e., the recovery of the AF phase on hundreds of picoseconds, an exponential decay of the FM phase on a 220 ps timescale

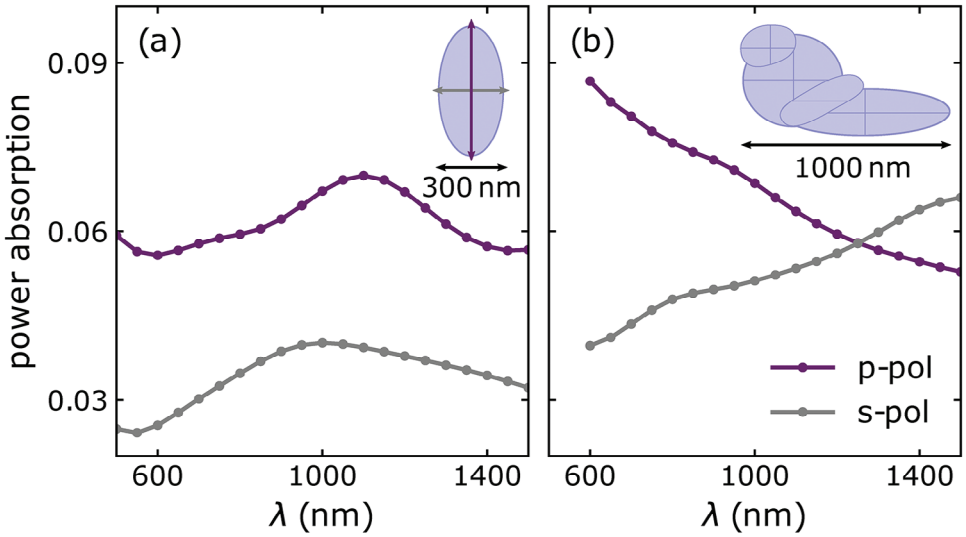

Figure 6. Spectral absorption of FeRh nanoislands calculated with COMSOL: a) Absorption spectrum of an ellipsoidal FeRh nanoisland for p- or s-polarized light incident within the *x-z* plane under 60 ° with respect to the surface normal. b) The same for a selected nanoisland of the investigated sample consisting of several ellipsoids leading to an irregular shape. We find a clear plasmonic resonance peak for the regularly shaped nanoislands at different wavelength λ for p- and s-polarization. As a superposition of structures with different resonance wavelengths, the absorption of the irregularly shaped nanoisland is grey. The insets show the structures consisting of ellipsoids with two principal axes highlighted by solid lines.

was empirically assumed, after the local temperature falls below the average FM-AF transition temperature $T_{FM\text{-}AF} = 350$ K (see Figure 1e).

Modelling of the Light Absorption via Finite Element Analysis: To understand the light absorption features of the nanostructured FeRh sample, the experimental $5 \times 5\ \mu m^2$ AFM topography data of the nanoislands were approximated by 220 (half-) ellipsoids utilizing an algorithm for rapid contour detection.[49] The ellipsoids resembling the topography of the sample were imported into the COMSOL Multiphysics 6.1 simulation software using a 10 and 5 nm discretization mesh along the lateral and vertical directions of the sample, respectively. Maxwell's equations were solved by the COMSOL RF module assuming a p-polarized light wave with a wavelength of $\lambda = 1028$ nm incident at 60° with respect to the sample normal and utilizing the refractive index of MgO refractive index of MgO[50] $n_{MgO} = 1.72$ and of FeRh $n_{FeRh} = 4.67 + 5.58i$ measured via spectroscopic ellipsometry at the pump laser wavelength. In a first calculation step, the background field coming from the vacuum-substrate system is obtained using periodic boundary conditions. Subsequently, the scattering field from the FeRh nanoislands is attained by bounding the computational domain to a perfectly matched layer. The simulation output consists of the spatially resolved absorbed power $P_{abs}(x, y, z)$ and electric field amplitude $E(x, y, z)$ in the modelled sample grid.

Figure 6a,b displays the COMSOL modelled absorption spectra for a regularly and an irregularly shaped nanoislands in the sample, respectively. As in the modelling in Figure 4, the light wave is incident in the *x*-*z* plane at 60° with respect to the surface normal (*z* axis). The insets display the nanostructures of different size and in-plane aspect ratio. For the nanoislands described by a single ellipsoid in Figure 6a the modelled absorption spectrum shows a distinct peak. Its spectral position differs between p- and s-polarization due to the different dimensions of the principle axis along *x* and *y*. The enhanced absorption within the narrow wavelength range indicated the excitation of plasmons in such FeRh nanoislands. The absorption spectrum of the irregularly shaped nanoislands could be understood as a superposition of several plasmonic peaks with different resonance wavelength, which rendered the absorption spectrum rather grey.

Acknowledgements

The authors acknowledged the DFG for financial support via Project-No. 328545488 – TRR 227 project A10 and the BMBF for funding via 05K22IP1. Access to the CEITEC Nano Research Infrastructure was supported by the Ministry of Education, Youth and Sports (MEYS) of the Czech Republic under the project CzechNanoLab (LM2023051). Measurements were carried out at the KMC3-XPP instrument at the BESSY II electron storage ring operated by the Helmholtz-Zentrum Berlin für Materialien und Energie. Funded by the Deutsche Forschungsgemeinschaft (DFG, German Research Foundation) - Projektnummer 491466077.

Open access funding enabled and organized by Projekt DEAL.

Conflict of Interest

The authors declare no conflict of interest.

Data Availability Statement

The data that support the findings of this study are available from the corresponding author upon reasonable request.

Keywords

phase transitions, plasmons, thin films, ultrafast magnetism, ultrafast X-ray diffraction

Received: October 20, 2023
Revised: April 16, 2024
Published online: May 14, 2024

[1] V. V. Temnov, G. Armelles, U. Woggon, D. Guzatov, A. Cebollada, A. Garcia-Martin, J.-M. Garcia-Martin, T. Thomay, A. Leitenstorfer, R. Bratschitsch, *Nat. Photonics* **2010**, *4*, 107.
[2] G. Armelles, A. Cebollada, A. García-Martín, M. U. González, *Adv. Opt. Mater.* **2013**, *1*, 10.
[3] D. Bossini, V. I. Belotelov, A. K. Zvezdin, A. N. Kalish, A. V. Kimel, *ACS Photonics* **2016**, *3*, 1385.
[4] D. Ignatyeva, C. Davies, D. Sylgacheva, A. Tsukamoto, H. Yoshikawa, P. Kapralov, A. Kirilyuk, V. Belotelov, A. Kimel, *Nat. Commun.* **2019**, *10*, 4786.
[5] M. Vergès, S. Perumbilavil, J. Hohlfeld, F. Freire-Fernández, Y. Le Guen, N. Kuznetsov, F. Montaigne, G. Malinowski, D. Lacour, M. Hehn, S. van Dijken, S. Mangin, *Adv. Sci.* **2023**, *10*, 2204683.
[6] F. Cheng, C. Wang, Z. Su, X. Wang, Z. Cai, N. X. Sun, Y. Liu, *Nano Lett.* **2020**, *20*, 6437.
[7] R. Rottmayer, S. Batra, D. Buechel, W. A. Challener, J. Hohlfeld, Y. Kubota, L. Li, B. Lu, C. Mihalcea, K. Mountfield, K. Pelhos, C. Peng, T. Rausch, M. A. Seigler, D. Weller, X.-M. Yang, *IEEE Trans. Magn.* **2006**, *42*, 2417.
[8] D. Weller, G. Parker, O. Mosendz, A. Lyberatos, D. Mitin, N. Y. Safonova, M. Albrecht, *J. Vac. Sci. Technol., B* **2016**, *34*, 060801.
[9] P. W. Granitzka, E. Jal, L. L. Guyader, M. Savoini, D. J. Higley, T. Liu, Z. Chen, T. Chase, H. Ohldag, G. L. Dakovski, W. F. Schlotter, S. Carron, M. C. Hoffman, A. X. Gray, P. Shafer, E. Arenholz, O Hellwig, V. Mehta, Y. K. Takahashi, J. Wang, E. E. Fullerton, J. Stöhr, A. H. Reid, H. A. Dürr, *Nano Lett.* **2017**, *17*, 2426.
[10] J.-U. Thiele, S. Maat, E. E. Fullerton, *Appl. Phys. Lett.* **2003**, *82*, 2859.
[11] L. Lewis, C. Marrows, S. Langridge, *J. Phys. D: Appl. Phys.* **2016**, *49*, 323002.
[12] Z. Feng, H. Yan, Z. Liu, *Adv. Electron. Mater.* **2019**, *5*, 1800466.
[13] I. Fina, J. Fontcuberta, *J. Phys. D: Appl. Phys.* **2019**, *53*, 023002.
[14] X. Zhu, Y. Xu, C. Cao, T. Shang, Y. Xie, Q. Zhan, *J. Phys.: Condens. Matter* **2022**, *34*, 144004.
[15] V. Uhlíř, J. A. Arregi, E. E. Fullerton, *Nat. Commun.* **2016**, *7*, 13113.
[16] J. A. Arregi, M. Horký, K. Fabianová, R. Tolley, E. E. Fullerton, V. Uhlíř, *J. Phys. D: Appl. Phys.* **2018**, *51*, 105001.
[17] J. A. Arregi, O. Caha, V. Uhlíř, *Phys. Rev. B* **2020**, *101*, 174413.
[18] R. Cherifi, V. Ivanovskaya, L. Phillips, A. Zobelli, I. Infante, E. Jacquet, V. Garcia, S. Fusil, P. Briddon, N. Guiblin, A. Mougin, A. A. Ünal, F. Kronast, S. Valencia, B. Dkhil, A. Barthélémy, M. Bibes, *Nat. Mater.* **2014**, *13*, 345.
[19] L. Motyčková, J. A. Arregi, M. Staňo, S. Průša, K. Částková, V. Uhlíř, *ACS Appl. Mater. Interfaces* **2023**, *15*, 8653.
[20] M. Mattern, A. von Reppert, S. P. Zeuschner, M. Herzog, J.-E. Pudell, M. Bargheer, *Photoacoustics* **2023**, *31*, 100503.
[21] A. von Reppert, L. Willig, J.-E. Pudell, M. Rössle, W. Leitenberger, M. Herzog, F. Ganss, O. Hellwig, M. Bargheer, *Appl. Phys. Lett.* **2018**, *113*, 123101.
[22] A. von Reppert, L. Willig, J.-E. Pudell, S. Zeuschner, G. Sellge, F. Ganss, O. Hellwig, J. Arregi, V. Uhlíř, A. Crut, M. Bargheer, *Sci. Adv.* **2020**, *6*, eaba1142.
[23] A. Reid, X. Shen, P. Maldonado, T. Chase, E. Jal, P. Granitzka, K. Carva, R. Li, J. Li, L. Wu, T. Vecchione, T. Liu, Z. Chen, D. J. Higley, N. Hartmann, R. Coffee, J. Wu, G. L. Dakovski, W. F. Schlotter, H. Ohldag, Y. K. Takahashi, V. Mehta, O. Hellwig, A. Fry, Y. Zhu, J. Cao, E. E. Fullerton, J. Stöhr, P. M. Oppeneer, X. J. Wang, et al., *Nat. Commun.* **2018**, *9*, 388.
[24] W.-S. Chang, F. Wen, D. Chakraborty, M.-N. Su, Y. Zhang, B. Shuang, P. Nordlander, J. E. Sader, N. J. Halas, S. Link, *Nat. Commun.* **2015**, *6*, 7022.
[25] G. Ju, J. Hohlfeld, B. Bergman, R. J. van de Veerdonk, O. N. Mryasov, J.-Y. Kim, X. Wu, D. Weller, B. Koopmans, *Phys. Rev. Lett.* **2004**, *93*, 197403.

[26] B. Bergman, G. Ju, J. Hohlfeld, R. J. van de Veerdonk, J.-Y. Kim, X. Wu, D. Weller, B. Koopmans, *Phys. Rev. B* **2006**, *73*, 060407.
[27] I. Radu, C. Stamm, N. Pontius, T. Kachel, P. Ramm, J.-U. Thiele, H. Dürr, C. Back, *Phys. Rev. B* **2010**, *81*, 104415.
[28] G. Li, R. Medapalli, J. Mentink, R. Mikhaylovskiy, T. Blank, S. Patel, A. Zvezdin, T. Rasing, E. Fullerton, A. Kimel, *Nat. Commun.* **2022**, *13*, 2998.
[29] F. Pressacco, D. Sangalli, V. Uhlíř, D. Kutnyakhov, J. A. Arregi, S. Y. Agustsson, G. Brenner, H. Redlin, M. Heber, D. Vasilyev, J. Demsar, G. Schönhense, M. Gatti, A. Marini, W. Wurth, F. Sirotti, *Nat. Commun.* **2021**, *12*, 5088.
[30] K. Kang, H. Omura, D. Yesudas, O. Lee, K.-J. Lee, H.-W. Lee, T. Taniyama, G.-M. Choi, *Nat. Commun.* **2023**, *14*, 3619.
[31] S. O. Mariager, F. Pressacco, G. Ingold, A. Caviezel, E. Möhr-Vorobeva, P. Beaud, S. Johnson, C. Milne, E. Mancini, S. Moyerman, E. Fullerton, R. Feidenhans'l, C. H. Back, C. Quitmann, *Phys. Rev. Lett.* **2012**, *108*, 087201.
[32] F. Quirin, M. Vattilana, U. Shymanovich, A.-E. El-Kamhawy, A. Tarasevitch, J. Hohlfeld, D. von der Linde, K. Sokolowski-Tinten, *Phys. Rev. B* **2012**, *85*, 020103.
[33] M. Mattern, J. Jarecki, J. A. Arregi, V. Uhlíř, M. Rössle, M. Bargheer, Disentangling nucleation and domain growth during a laser-induced phase transition. APL Materials **2024**, https://doi.org/10.1063/5.0206095.
[34] L. Willig, A. von Reppert, M. Deb, F. Ganss, O. Hellwig, M. Bargheer, *Phys. Rev. B* **2019**, *100*, 224408.
[35] M. Rössle, W. Leitenberger, M. Reinhardt, A. Koç, J. Pudell, C. Kwamen, M. Bargheer, *J. Synchrotron Radiat.* **2021**, *28*, 948.
[36] F. Pressacco, V. Uhlíř, M. Gatti, A. Bendounan, E. E. Fullerton, F. Sirotti, *Sci. Rep.* **2016**, *6*, 22383.
[37] R. Fan, C. J. Kinane, T. Charlton, R. Dorner, M. Ali, M. De Vries, R. M. Brydson, C. H. Marrows, B. J. Hickey, D. A. Arena, B. K. Tanner, G. Nisbet, S. Langridge, *Phys. Rev. B* **2010**, *82*, 184418.
[38] L. Zsoldos, *Phys. Status Solidi B* **1967**, *20*, K25.
[39] G. Laskin, H. Wang, H. Boschker, W. Braun, V. Srot, P. A. van Aken, J. Mannhart, *Nano Lett.* **2019**, *19*, 1131.
[40] F. J. Garcia-Vidal, A. I. Fernández-Domínguez, L. Martin-Moreno, H. C. Zhang, W. Tang, R. Peng, T. J. Cui, *Rev. Mod. Phys.* **2022**, *94*, 025004.
[41] U. Kreibig, M. Vollmer, *Optical properties of metal clusters*, vol. *25*, Springer Science & Business Media, Berlin, Heidelberg **2013**.
[42] S. A. Maier, et al., *Plasmonics: fundamentals and applications*, vol. *1*, Springer, Berlin, Heidelberg **2007**.
[43] I. Zoric, M. Zach, B. Kasemo, C. Langhammer, *ACS Nano* **2011**, *5*, 2535.
[44] K. L. Kelly, E. Coronado, L. L. Zhao, G. C. Schatz, *J. Phys. Chem. B* **2003**, *107*, 668.
[45] L.-Y. Chen, D. W. Lynch, *Phys. Rev. B* **1988**, *37*, 10503.
[46] J. Y. Rhee, D. W. Lynch, *Phys. Rev. B* **1995**, *51*, 1926.
[47] V. Saidl, M. Brajer, L. Horák, H. Reichlová, K. Výborný, M. Veis, T. Janda, F. Trojánek, M. Maryško, I. Fina, X. Marti, T. Jungwirth, P. Němec, *New J. Phys.* **2016**, *18*, 083017.
[48] M. Ibarra, P. Algarabel, *Phys. Rev. B* **1994**, *50*, 4196.
[49] C. Rasche, *IET Image Process.* **2018**, *12*, 532.
[50] R. E. Stephens, I. H. Malitson, *J. Res. Natl. Bur. Stand.* **1952**, *49*, 249.